

# Strengthening Brittle Semiconductor Nanowires through Stacking Faults: Insights from in Situ Mechanical Testing

Bin Chen,<sup>†</sup> Jun Wang,<sup>‡</sup> Qiang Gao,<sup>§</sup> Yujie Chen,<sup>†</sup> Xiaozhou Liao,<sup>\*,†</sup> Chunsheng Lu,<sup>\*,||</sup> Hark Hoe Tan,<sup>§</sup> Yiu-Wing Mai,<sup>†</sup> Jin Zou,<sup>⊥</sup> Simon P. Ringer,<sup>†,#</sup> Huajian Gao,<sup>∇</sup> and Chennupati Jagadish<sup>§</sup>

<sup>†</sup>School of Aerospace, Mechanical and Mechatronic Engineering, The University of Sydney, Sydney, New South Wales 2006, Australia

<sup>‡</sup>State Key Laboratory of Nonlinear Mechanics (LNM), Institute of Mechanics, Chinese Academy of Sciences, Beijing 100190, China

<sup>§</sup>Department of Electronic Materials Engineering, Research School of Physics and Engineering, The Australian National University, Canberra, Australian Capital Territory 0200, Australia

<sup>||</sup>Department of Mechanical Engineering, Curtin University, Perth, Western Australia 6845, Australia

<sup>⊥</sup>Materials Engineering and Centre for Microscopy and Microanalysis, The University of Queensland, St. Lucia, Queensland 4072, Australia

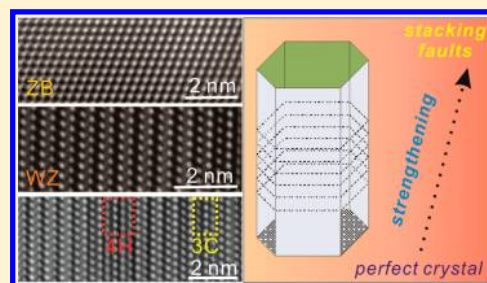
<sup>#</sup>Australian Centre of Microscopy and Microanalysis, The University of Sydney, Sydney, New South Wales 2006, Australia

<sup>∇</sup>School of Engineering, Brown University, Providence, Rhode Island 02912, United States

## S Supporting Information

**ABSTRACT:** Quantitative mechanical testing of single-crystal GaAs nanowires was conducted using in situ deformation transmission electron microscopy. Both zinc-blende and wurtzite structured GaAs nanowires showed essentially elastic deformation until bending failure associated with buckling occurred. These nanowires fail at compressive stresses of  $\sim 5.4$  GPa and 6.2 GPa, respectively, which are close to those values calculated by molecular dynamics simulations. Interestingly, wurtzite nanowires with a high density of stacking faults fail at a very high compressive stress of  $\sim 9.0$  GPa, demonstrating that the nanowires can be strengthened through defect engineering. The reasons for the observed phenomenon are discussed.

**KEYWORDS:** GaAs nanowires, strengthening, stacking fault, in situ deformation, molecular dynamics, transmission electron microscopy



The strength of a material refers to the largest stress that the material can withstand without failure. Metallic materials are generally ductile where the stress–strain curves contain an elastic deformation region and a subsequent plastic region before fracture in response to an applied load. The strength of crystalline metallic materials can be tailored through alloying, work-hardening, and any other mechanisms that hinder dislocation motion.<sup>1–6</sup> For brittle ceramics, there is usually no dislocation slip, and substantial research efforts have been focused on increasing the fracture toughness by delaying the formation and propagation of cracks. In comparison to metallic materials, much less attention has been paid to the strengthening of brittle materials.

With the rapid development of novel devices at the micro- and nanoscales, many investigations of nanostructures including semiconductor nanowires (NWs) have emerged due to their unique electrical, optical, and mechanical properties that can be used in a wide variety of electronic, optoelectronic, and electromechanical applications.<sup>7–13</sup> To realize the integration of NWs into NW-based devices, the mechanical behavior of NWs needs to be addressed. Although the synthesis/growth and optoelectronic properties of NWs have been extensively studied, their mechanical properties and underlying deforma-

tion mechanisms are considerably overlooked due to the difficulty of mechanical characterization of nanoscale objects. It has been reported that mechanical strain strongly affects the electrical, optical, and magnetic properties of nanomaterials.<sup>14–16</sup> In addition, semiconductor NWs can possess different crystal structures, such as the cubic zinc-blende (ZB, 3C) and the hexagonal wurtzite (WZ, 2H) structures, and the NWs may contain various crystalline defects like stacking faults (SFs) and twins.<sup>17,18</sup> Exploring the mechanical behavior of semiconductor NWs and how it is affected by the microstructure are important because the reliability and even functionality of NW-based devices depend on the mechanical properties of the NWs.

Following the recent advances of in situ deformation transmission electron microscopy (TEM),<sup>19–25</sup> it is now possible to simultaneously conduct mechanical testing and structural characterization of nanostructured samples to explore their fundamental properties at the nanoscale. In this Letter, the mechanical properties of GaAs NWs are investigated by using an in situ deformation TEM technique. Surprisingly, it is found

**Received:** June 16, 2013

**Revised:** August 20, 2013

**Published:** August 28, 2013

that the presence of SFs in GaAs NWs can substantially increase the loading capacity of the NWs before failure. This phenomenon has not been reported in bulk GaAs samples previously and is also unexpected since SFs are usually regarded as weak sites in semiconductor materials.<sup>26</sup> The reasons for such strengthening in NWs will be discussed.

Single crystal GaAs NWs were epitaxially grown on GaAs (111)<sub>B</sub> substrates using Au nanoparticles as catalyst by metal–organic chemical vapor deposition. Trimethylgallium and AsH<sub>3</sub> were used as precursors together with ultrahigh purity hydrogen as the carrier gas. To explore the effects of crystal structures and defects on the mechanical behavior, three kinds of NWs were prepared, each having a different microstructure: ZB, WZ, and WZ with a high density of SFs, fabricated by controlling the growth temperature. A detailed description regarding the growth of GaAs NWs has been reported elsewhere.<sup>27,28</sup> The morphology of GaAs NWs was characterized using a ZEISS Auriga scanning electron microscope (SEM). SEM characterization showed that the cross sections of the NWs are of hexagonal geometry. This was used to calculate the cross-sectional area for stress evaluation. High-resolution structural characterization of NWs was performed using a JEOL JEM-3000F TEM.

For mechanical testing, the samples consisting of the NWs grown on the substrate were mounted on a Hysitron PicoIndenter holder (PI 95) inside a JEOL JEM-2100 TEM. In situ compression of the NWs was applied using the PicoIndenter with a flat diamond punch under the displacement-controlled mode. The full deformation process was recorded by TEM images and real-time video at a speed of 30 frames per second. For convenience of comparison, engineering stress defined as applied load per unit cross-sectional area on a NW was used. For each kind of structures, about 10 NWs were tested to obtain meaningful statistical values.

Additional insights were obtained by comparing the experimental observations with molecular dynamics (MD) simulations. In MD simulations, a modified Tersoff potential was used to model atomic interactions.<sup>29</sup> NWs with 3C, 2H, and 4H structures were generated by stacking the tetrahedral bonding of Ga–As with sequences of “ABC...”, “ABAB...”, and “ABAC...”, respectively. 2H NWs with SFs were prepared by randomly inserting 3C and 4H units into the 2H matrix, with distance between neighboring SFs being 1, 3, 5, 7, and 10 nm. To simulate compressive loading, a strain was applied along the axis of a NW in two steps. First, the NW was compressed by an isobaric ensemble at a strain rate of  $-0.001 \text{ ps}^{-1}$  for 1 ps; then, the axial strain was fixed while the NW was relaxed for 6 ps through a canonical ensemble. The system temperature was maintained at 300 K. Samples were relaxed for 20 ps before compression was applied. Stress was calculated by the classical virial formula. All calculations were performed using the DL\_POLY2.20 package.<sup>30</sup> More details about MD simulations can be found elsewhere.<sup>31,32</sup>

GaAs NWs with three kinds of structures—ZB, WZ, and WZ with a high density of SFs (hereafter named WZ–SF NWs)—were grown and tested to explore their mechanical behaviors. Only the NWs with the same diameter ( $\sim 60 \text{ nm}$ ) were illustrated in this work for the following reasons: (1) the NWs with large diameters have relatively low strengths, which obeys the general size effect that “smaller is stronger”;<sup>33–35</sup> (2) it is difficult to detect experimentally the small load applied to NWs with very small diameters because of the poor signal-to-noise

ratio; and (3) as will be shown later, the ultimate loading capacities of NWs with a diameter of  $\sim 60 \text{ nm}$  are very close to their failure stresses calculated by MD simulations.

Figure 1 shows the structures of the three types of as-grown GaAs NWs of diameter  $\sim 60 \text{ nm}$ . Typical low magnification

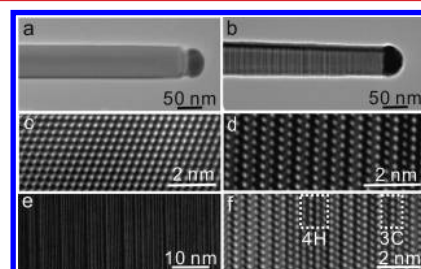


**Figure 1.** (a) A typical low magnification TEM image of a GaAs NW without any SF; (b) a typical TEM image of a GaAs NW with a high density of SFs; (c–d) high-resolution TEM images of GaAs NWs with ZB and WZ structures, respectively; (e) a high-resolution TEM image of a WZ NW with a high density of SFs; and (f) an enlarged typical high-resolution TEM image obtained from an area in part e.

TEM images of the NWs without and with SFs are presented in Figure 1a and b, respectively. In all cases, an Au catalytic nanoparticle is located at the tip of each NW. No obvious tapering is seen in these NWs. High-resolution TEM characterization reveals three kinds of microstructures in the NWs. The NW in Figure 1c has a stacking sequence of “ABCABC...”, corresponding to a pure 3C ZB structure. The stacking sequence of the NW in Figure 1d is “ABAB...”, indicating a 2H WZ structure. Finally, the NW in Figure 1e shows a 2H WZ structure with a high density of SFs (WZ–SF) which appear as stripes in the image. The distances between the neighboring SFs are in the range of  $\sim 1\text{--}5 \text{ nm}$ . The SFs are categorized as polytypic inclusions according to their local stacking orders. The most common inclusions are designated as 3C and 4H located inside the 2H matrix, whose typical high-resolution TEM image is shown in Figure 1f.

In situ compression tests were conducted to investigate the effects of the crystalline structures and defects on the mechanical behavior of NWs. Figure 2 shows the load–displacement curves and a series of in situ deformation TEM images extracted from Movies 1–3 in the Supporting Information. The NWs have a diameter of  $\sim 60 \text{ nm}$  with an aspect ratio of length-to-diameter  $\sim 6.5:1$ . Figure 2a plots the load–displacement curve for a ZB-structured NW whose initial state before compression is shown in Figure 2b. When the diamond punch moved toward the NW, the NW experienced a force during the loading process. A maximum force of  $\sim 10 \mu\text{N}$  occurs (see Figure 2a) just before the NW fails (Figure 2c). The same experimental procedure was applied to WZ and WZ–SF NWs. The load–displacement curves and the corresponding deformation images of a WZ NW (row 2) and a WZ–SF NW (row 3) are presented in Figure 2d–f and g–i, respectively. The TEM images in Figure 2e,h and 2f,i correspond to the states of the NWs before applying compression and immediately before failure, respectively. The NW with the WZ structure fails at a force of  $\sim 15 \mu\text{N}$ . Surprisingly, the WZ–SF NW fails at a force of  $\sim 22 \mu\text{N}$ , which is much larger than those of the NWs with the ZB or WZ structure.

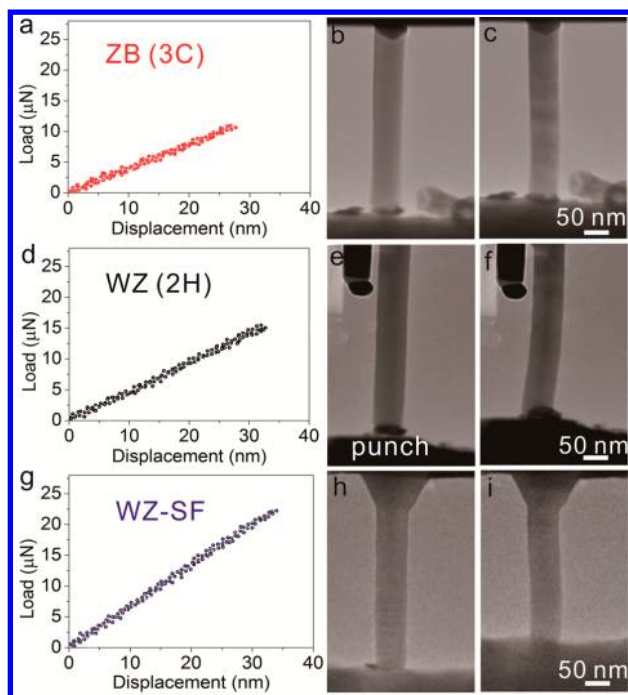


**Figure 2.** In situ mechanical testing of ZB, WZ, and WZ-SF GaAs NWs with a diameter of  $\sim 60$  nm and an aspect ratio of length-to-diameter of  $\sim 6.5:1$ . (a) Load–displacement curve of a ZB NW; (b–c) the corresponding TEM images extracted from Movie 1 in the Supporting Information showing the NW in the initial state (b) and buckling-induced bending before fracture (c); (d) load–displacement curve of a WZ NW; (e–f) the corresponding TEM images extracted from Movie 2 in the Supporting Information; (g) load–displacement curve of a WZ NW with dense SFs; and (h–i) the corresponding TEM images extracted from Movie 3 in the Supporting Information. The images in the middle and right columns correspond to the states of the NWs before compression and at buckling-induced bending just prior to failure, respectively.

To assess if buckling occurred in a NW, an analysis was conducted using the Euler formula. The critical load, that is, the load  $P_{cr}$  at which the NW can buckle is given by,

$$P_{cr} = \frac{\pi^2 EI}{(KL)^2}$$

where  $E$  is Young's modulus,  $I$  is the area moment of inertia ( $I = [(5\sqrt{3})/16]r^4$  for the NW hexagonal cross section with a side length of  $r$ ),  $L$  is the length of the NW, and  $K$  is a factor accounting for the boundary conditions ( $K = 0.5$  was used in the calculation).

By using the NW dimensions and the load–displacement curve in Figure 2a, the Young's modulus was estimated to be  $E = 76.5$  GPa for the ZB NW. Based on the Euler equation, the buckling load  $P_{cr} = 10.3 \pm 0.5$   $\mu$ N, which is close to but slightly higher than the maximum load ( $\sim 10$   $\mu$ N) shown in Figure 2a. Similarly, for the other two cases in Figure 2d and g, the maximum loads ( $\sim 15$   $\mu$ N and  $22$   $\mu$ N) for WZ and WZ-SF NWs are also similar to their respective Euler buckling loads ( $14.9 \pm 0.7$   $\mu$ N and  $23.5 \pm 1.2$   $\mu$ N, respectively). From these results, it can be inferred that all three types of NWs (with an aspect ratio of  $\sim 6.5$ ) undergo a transition from mainly compression to buckling at the maximum load. Failure by buckling-induced bending occurs as shown in Figure 2c, f, and i. The loading capacities of the ZB, WZ, and WZ-SF NWs may be conveniently calculated as ultimate compressive stresses with

the values of  $\sim 5.4$ ,  $6.2$ , and  $9.0$  GPa, respectively, just before failure. Therefore, the NWs with a high density of SFs have the highest loading capacity. The deformation and failure behaviors of NWs with larger aspect ratios are dominated by bending, which are discussed in the Supporting Information.

MD simulations were performed to obtain a better understanding of the loading capacities of GaAs NWs. Figure 3a shows the atomic arrangements of ZB (3C) and WZ (2H)

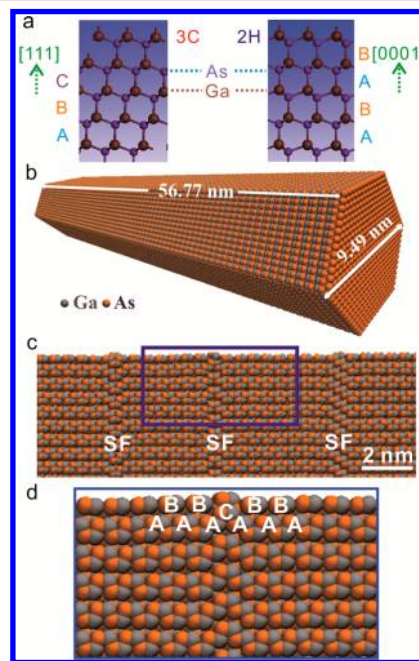


**Figure 3.** (a) Atomic configurations of GaAs with the ZB and WZ structures; (b) a computational model used in MD simulations, where the aspect ratio of length to diameter is  $\sim 6:1$ ; (c) a model used in MD simulations for investigating the SF effect; and (d) a detailed view of the local SF structure that is marked with a rectangle in (c).

GaAs structures for a conceptual understanding. When the vertical Ga–As bond is treated as a unit, the 3C structure has the stacking sequence of “ABCABC...”, while the 2H has the stacking sequence of “ABAB...”. A sample with a length of  $56.8$  nm and a diameter of  $9.5$  nm (thus having an aspect ratio of  $\sim 6:1$ , similar to that used in the experiments) was used in the MD simulations (Figure 3b). To investigate the SF effect, a number of SFs were inserted into the 2H matrix, such as the structure with a neighboring SF distance of  $5$  nm shown in Figure 3c. A marked rectangular region is enlarged in Figure 3d, showing a 4H inclusion inside the 2H matrix. The available potential function of GaAs common polytypes such as 2H, 3C, and 4H was used in the MD simulations.<sup>29</sup>

The simulation results are shown in Figure 4. In Figure 4a, GaAs NWs with the ZB (3C) and WZ (2H) structures fail after reaching the ultimate compressive stresses of  $\sim 5.6$  and  $6.4$  GPa (Figure 4a), respectively, in good agreement with the corresponding experimental results of  $\sim 5.4$  and  $6.2$  GPa. These values are, however, very much higher than the corresponding bulk strength (hundreds of MPa).<sup>36</sup> Such behavior is similar to that observed in other materials, which follows the general trend of “smaller is stronger”.<sup>33–35</sup> In brittle materials like GaAs, the failure process involves the initiation and growth of cracks. Crack initiation usually occurs at small flaws on the surface or inside the material. The probability of

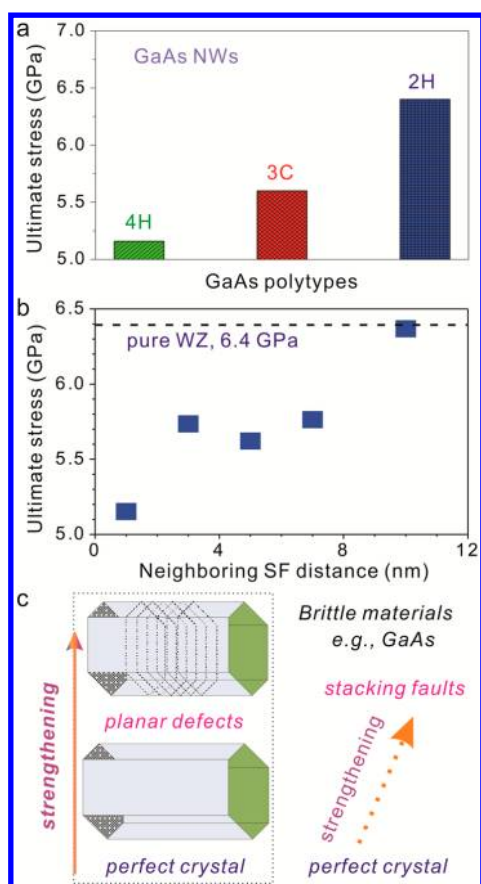


**Figure 4.** (a) MD simulation results showing the ultimate compressive stresses of 3C, 2H, and 4H GaAs polytypes; (b) the ultimate compressive stress of 2H WZ-SF NWs with the neighboring SF distances ranging from 1 to 10 nm; and (c) strengthening in brittle materials through defect engineering (via insertion of planar defects).

the existence of a flaw that is able to initiate a crack decreases when the physical dimensions of a brittle material are reduced. Hence, with the sample size reducing to the nanoscale range, that is, several tens of nanometers, crack initiation in the NWs is difficult thus allowing them to sustain stresses approaching the theoretical values.

For WZ-SF samples, a very high density of SFs with polytypes including 3C and 4H are inserted into the 2H matrix. MD simulations show that the compressive failure stresses of 3C and 4H are both lower than that of 2H (Figure 4a) and that mixing 3C and 4H into the 2H structure leads to strength weakening (Figure 4b). Specifically, when the distance between neighboring SFs is reduced from 10 to 1 nm, the failure stress decreases from ~6.4 to 5.2 GPa. This is opposite to the experimental results. The variation of bond arrangement at the SF sites is considered an important factor for the high strength of GaAs NWs with a high density of SFs. Bond stretch or shrinkage in materials leads to the deformation of materials during loading process. It has been shown from simulations that the bond strength depends on the location of bonds.<sup>37</sup> This implies that the bond strength varies at the A, B, or C stacking sites. The various possible arrangements of bonds stacking at the dense SF sites may change the local interatomic interaction and, consequently, alter the strength of bonds. Since the NW contains a high density of almost evenly spaced SFs (at about 1–5 nm), the collective behavior of a huge number of bonds at the SF sites controls the strength of the NW.

Unfortunately, the MD potential function<sup>29</sup> was established based on several common GaAs polymorphs such as 2H, 3C, and 4H. While it describes the bond strength of these common polymorphs well, it fails to predict the bond strength at various SF sites in a 2H NW because it is difficult to adopt an appropriate potential function to describe all possible SF structures and the corresponding interfacial states.

Since the length-to-diameter aspect ratios and the diameters of the three types of NWs are similar, the highest loading capacity of the WZ-SF NW is due to its highest Young's modulus. The extremely high density of SFs in the WZ-SF NWs leads to the formation of various polytypic structures in the NWs. Similar to the situation in which different polytypic SiC structures have different Young's moduli,<sup>38,39</sup> the Young's moduli of different GaAs polytypic structures are also different. This is confirmed from the different slopes of the linear elastic load–displacement curves in Figure 2. Although all NWs were initially adjusted normal to the punch, slight misalignment may be unavoidable during the deformation process. However, previous work by Zhu and Espinosa<sup>40</sup> showed that misalignment of ~5° resulted in only <1% difference of the Young's modulus. Our experimental results demonstrate that the loading capacity of WZ-SF samples is larger than those of all other samples, which is interesting since material strengthening can be realized in a brittle material through the inclusion of SF defects.

As indicated, the final failure of the NWs is due to buckling-induced bending. The effect of SFs in suppressing crack initiation can also play an important role in increasing the failure stress of GaAs NWs. Compared to NWs with perfect structures, the NWs with a high density of SFs are stiffer (that is, higher Young's modulus) and hence are more resistant to bending. As a result, crack initiation is better suppressed in the NWs with a high density of SFs, which leads to a larger applied stress before failure occurs. Our experimental results imply that the widely accepted engineering concept of stress concentration at SFs<sup>41</sup> is no longer valid if the density of SFs is significantly high (spacing between neighboring SFs is only several nanometers).

It is known from ductile metals such as Cu that nanopillars with a large number of planar nanotwins have a higher strength than the single crystalline form.<sup>5,6,42</sup> The twin spacing in those nanotwinned nanopillars is comparable to the SF spacing in the present study. Strengthening in nanotwinned Cu is attributed to the impedance of the passage of gliding dislocations by twin boundaries.<sup>43</sup> For brittle WZ-SF NWs demonstrated in Figure 4c, the distance between neighboring SFs in the NWs is only 1–5 nm. The arrangement of such a huge number of SFs in the NWs changes the bond strength at the interfacial sites and thus the ultimate loading capacity of the NWs. It should be noted that, however, the GaAs NWs with numerous SFs remain in a single crystalline form, which is different from the polycrystalline Cu pillars with nanotwins. It is intriguing that a brittle material, such as GaAs NWs, can be strengthened through the introduction of a high density of planar defects with distances of several nanometers into the matrix.

In summary, quantitative in situ TEM experiments show that the deformation behaviors of ZB, WZ, and WZ-SF GaAs NWs under compression are elastic till the maximum load, whence buckling-induced bending failure occurs. These NWs fail at ultimate compressive stresses of ~5.4, 6.2, and 9.0 GPa, respectively. The values of ZB and WZ NWs are close to those calculated by MD simulations. But an unusually high failure

stress is achieved in NWs with a high density of SFs (WZ–SF) attributed to their high Young's modulus values and the SFs which hinder crack initiation. These findings have pointed to the potential of tuning the mechanical behavior of nanostructures with covalent/ionic bonding through planar defect engineering.

## ■ ASSOCIATED CONTENT

### ■ Supporting Information

Movies 1–3 from which the snapshot images extracted in Figure 2 and the deformation behavior of GaAs NWs with large aspect ratios and Movies 4–5. This material is available free of charge via the Internet at <http://pubs.acs.org>.

## ■ AUTHOR INFORMATION

### Corresponding Authors

\*E-mail: [xiaozhou.liao@sydney.edu.au](mailto:xiaozhou.liao@sydney.edu.au).

\*E-mail: [C.Lu@curtin.edu.au](mailto:C.Lu@curtin.edu.au).

### Notes

The authors declare no competing financial interest.

## ■ ACKNOWLEDGMENTS

We acknowledge for the scientific and technical input and support from the Australian Microscopy and Microanalysis Research Facility Node at the University of Sydney. We also thank the Australian National Fabrication Facility for providing access to growth facilities for the NWs used in this work. This research is supported by the Australian Research Council, the National Natural Science Foundation of China (Grant Nos. 11172024, 11232013 and 11372022), the China Postdoctoral Science Foundation (2012T50029), and the Opening Fund of State Key Laboratory of Nonlinear Mechanics. Simulations were conducted at iVEC through the use of advanced computing resources located at [iVEC@Murdoch](mailto:iVEC@Murdoch). Partially computational resources were provided by the Intersect Australia Ltd.

## ■ REFERENCES

- (1) Hassan, Kh. A. A.; Norman, A. F.; Price, D. A.; Prangnell, P. B. *Acta Mater.* **2003**, *51*, 1923–1936.
- (2) Sha, G.; Moller, H.; Stumpf, W. E.; Xia, J. H.; Govender, G.; Ringer, S. P. *Acta Mater.* **2012**, *60*, 692–701.
- (3) Kocks, U. F.; Mecking, H. *Prog. Mater. Sci.* **2003**, *48*, 171–273.
- (4) Ma, E.; Wang, Y. M.; Lu, Q. H.; Sui, M. L.; Lu, L.; Lu, K. *Appl. Phys. Lett.* **2004**, *85*, 4932–4934.
- (5) Lu, L.; Chen, X.; Huang, X.; Lu, K. *Science* **2009**, *323*, 607–610.
- (6) Jang, D. C.; Cai, C.; Greer, J. R. *Nano Lett.* **2011**, *11*, 1743–1746.
- (7) Tian, B. Z.; Zheng, X. L.; Kempa, T. J.; Fang, Y.; Yu, N. F.; Yu, G. H.; Huang, J. L.; Lieber, C. M. *Nature* **2007**, *449*, 885–890.
- (8) Wang, Z. L. *Mater. Sci. Eng. R* **2009**, *64*, 33–71.
- (9) Fang, X. S.; Bando, Y.; Liao, M. Y.; Gautam, U. K.; Zhi, C. Y.; Dierre, B.; Liu, B. D.; Zhai, T. Y.; Sekiguchi, T.; Koide, Y.; Golberg, D. *Adv. Mater.* **2009**, *21*, 2034–2039.
- (10) Lazzarini, L.; Salviati, G.; Fabbri, F.; Zha, M. Z.; Calestani, D.; Zappettini, A.; Sekiguchi, T.; Dierre, B. *ACS Nano* **2009**, *3*, 3158–3164.
- (11) Dai, X.; Dayeh, S. A.; Veeramuthu, V.; Larrue, A.; Wang, J.; Su, H. B.; Soci, C. *Nano Lett.* **2011**, *11*, 4947–4952.
- (12) Bar-Sadan, M.; Barthel, J.; Shtrikman, H.; Houben, L. *Nano Lett.* **2012**, *12*, 2352–2356.
- (13) Ganjipour, B.; Wallentin, J.; Borgstrom, M. T.; Samuelson, L.; Thelander, C. *ACS Nano* **2012**, *6*, 3109–3113.
- (14) Yang, R. S.; Qin, Y.; Dai, L. M.; Wang, Z. L. *Nat. Nanotechnol.* **2009**, *4*, 34–39.
- (15) Cao, J.; Ertekin, E.; Srinivasan, V.; Fan, W.; Huang, S.; Zheng, H.; Yim, J. W. L.; Khanal, D. R.; Ogetree, D. F.; Grossman, J. C.; Wu, J. *Nat. Nanotechnol.* **2009**, *4*, 732–737.
- (16) Pillarisetty, R. *Nature* **2011**, *479*, 324–328.
- (17) Joyce, H. J.; Wong-Leung, J.; Gao, Q.; Tan, H. H.; Jagadish, C. *Nano Lett.* **2010**, *10*, 908–915.
- (18) Joyce, H. J.; Gao, Q.; Tan, H. H.; Jagadish, C.; Kim, Y.; Zou, J.; Smith, L. M.; Jackson, H. E.; Yarrison-Rice, J. M.; Parkinson, P.; Johnston, M. B. *Prog. Quant. Electron.* **2011**, *35*, 23–75.
- (19) Han, X. D.; Zhang, Y. F.; Zheng, K.; Zhang, X. N.; Zhang, Z.; Hao, Y. J.; Guo, X. Y.; Yuan, J.; Wang, Z. L. *Nano Lett.* **2007**, *7*, 452–457.
- (20) Shan, Z. W.; Mishra, R. K.; Asif, S. A. S.; Warren, O. L.; Minor, A. M. *Nat. Mater.* **2008**, *7*, 115–119.
- (21) Yu, Q.; Shan, Z. W.; Li, J.; Huang, X. X.; Xiao, L.; Sun, J.; Ma, E. *Nature* **2010**, *463*, 335–338.
- (22) Lu, Y.; Huang, J. Y.; Wang, C.; Sun, S. H.; Lou, J. *Nat. Nanotechnol.* **2010**, *5*, 218–224.
- (23) Kiener, D.; Minor, A. M. *Acta Mater.* **2011**, *59*, 1328–1337.
- (24) Wang, Y. B.; Wang, L. F.; Joyce, H. J.; Gao, Q.; Liao, X. Z.; Mai, Y.-W.; Tan, H. H.; Zou, J.; Ringer, S. P.; Gao, H. J.; Jagadish, C. *Adv. Mater.* **2011**, *23*, 1356–1360.
- (25) Wang, Y. B.; Joyce, H. J.; Gao, Q.; Liao, X. Z.; Tan, H. H.; Zou, J.; Ringer, S. P.; Shan, Z. W.; Jagadish, C. *Nano Lett.* **2011**, *11*, 1546–1549.
- (26) Li, Z. J.; Wang, S. J.; Wang, Z. G.; Zu, X. T.; Gao, F.; Weber, W. J. *J. Appl. Phys.* **2010**, *108*, 013504.
- (27) Joyce, H. J.; Gao, Q.; Tan, H. H.; Jagadish, C.; Kim, Y.; Zhang, X.; Guo, Y.; Zou, J. *Nano Lett.* **2007**, *7*, 921–926.
- (28) Joyce, H. J.; Gao, Q.; Tan, H. H.; Jagadish, C.; Kim, Y.; Fickenscher, M. A.; Perera, S.; Hoang, T. B.; Smith, L. M.; Jackson, H. E.; Yarrison-Rice, J. M.; Zhang, X.; Zou, J. *Nano Lett.* **2009**, *9*, 695–701.
- (29) Fichtorn, K. A.; Tiwary, Y.; Hammerschmidt, T.; Kratzer, P.; Scheffler, M. *Phys. Rev. B* **2011**, *83*, 195328.
- (30) Smith, W.; Yong, C. W.; Rodger, P. M. *Mol. Simul.* **2002**, *28*, 385–471.
- (31) Wang, J.; Lu, C.; Wang, Q.; Xiao, P.; Ke, F. J.; Bai, Y. L.; Shen, Y. G.; Wang, Y. B.; Liao, X. Z.; Gao, H. J. *Europhys. Lett.* **2012**, *98*, 16010.
- (32) Wang, J.; Lu, C. S.; Wang, Q.; Xiao, P.; Ke, F. J.; Bai, Y. L.; Shen, Y. G.; Wang, Y. B.; Chen, B.; Liao, X. Z.; Gao, H. J. *Acta Mater.* **2012**, *60*, 5593–5600.
- (33) Gao, H. J.; Ji, B. H.; Jager, I. L.; Arzt, E.; Fratzl, P. *Proc. Natl. Acad. Sci. U.S.A.* **2003**, *100*, 5597–5600.
- (34) Zhu, T.; Li, J. *Prog. Mater. Sci.* **2010**, *55*, 710–757.
- (35) Greer, J. R.; De Hosson, J.; Th, M. *Prog. Mater. Sci.* **2011**, *56*, 654–724.
- (36) Wang, S. L.; Pirouz, P. *Acta Mater.* **2007**, *55*, 5500–5514.
- (37) Umeno, Y.; Kinoshita, Y.; Kitamura, T. *Model. Simul. Mater. Sci. Eng.* **2007**, *15*, 27–37.
- (38) Locke, C.; Kravchenko, G.; Waters, P.; Reddy, J. D.; Du, K.; Volinsky, A. A.; Frewin, C. L.; Sadow, S. E. *Mater. Sci. Forum* **2009**, *615–617*, 633–636.
- (39) Hossain, T. K.; MacLaren, S.; Engel, J. M.; Liu, C.; Adesida, H.; Okojie, R. S. *J. Micromesh. Microeng.* **2006**, *16*, 751–756.
- (40) Zhu, Y.; Espinosa, H. D. *Proc. Natl. Acad. Sci. U.S.A.* **2005**, *102*, 14503–14508.
- (41) Wu, X. L.; Zhu, Y. T. *Appl. Phys. Lett.* **2006**, *89*, 031922.
- (42) Jang, D. C.; Li, X. Y.; Gao, H. J.; Greer, J. R. *Nat. Nanotechnol.* **2012**, *7*, 594–601.
- (43) Li, X. Y.; Wei, Y. J.; Lu, L.; Lu, K.; Gao, H. J. *Nature* **2010**, *464*, 877–880.